

ARTICLE INFO:

Received : June 10, 2019

Revised : January 27, 2020

Accepted : April 08, 2020

CT&F - Ciencia, Tecnología y Futuro Vol 10, Num 1 June 2020. pages 93 - 106

DOI : 10.29047/01225383.163



ANALYSIS OF THE COVARIANCE MATRIX IN FWI THROUGH DENSITY OF COVARIANCE MAPS

■ ANÁLISIS DE LA MATRIZ DE COVARIANZA EN INVERSIÓN DE ONDA COMPLETA (FWI) A TRAVÉS DE MAPAS DE DENSIDAD DE COVARIANZA

Jiménez, Anyeres A.^{a*}; Muñoz-Cuartas, J. C.^a; Avendaño, Sheryl^a; Gómez, Leonardo^b

ABSTRACT

Full waveform inversion (FWI) is a tool for the inversion of seismic data. There are several sources of uncertainty in the results provided by FWI. The quantification of such uncertainties has been studied through the resolution matrix (**Res**), which rests on a quadratic approximation that interprets the Hessian matrix as the posterior covariance matrix. Despite efforts in the use of **Res**, there is no published analysis of the uncertainties contained in the full correlation matrix, (**R**). Our approach leads to build the full **R** matrix, which, at the end of the day, is the final quantity that includes all the information associated with uncertainties. We focused on uncertainties related to variation in the starting models of the FWI, and thus propose a method to study the full **R** matrix, which is called the Density of Correlation Map, **D**. By using the **D** map, we found that the highest uncertainty zones in the FWI inverted model are near the sources, the model boundaries, and the interfaces. We argue that **D** can be a complement for the study and estimation of uncertainties in FWI.

RESUMEN

a inversión por campo de onda completa (FWI) es una herramienta para la inversión de datos sísmicos. Hay varias fuentes de incertidumbre en los resultados proporcionados por FWI. La cuantificación de tales incertidumbres se ha estudiado a través de la matriz de resolución (**Res**), que se basa en una aproximación cuadrática que interpreta la matriz Hessiana como la matriz de covarianza posterior. A pesar de los esfuerzos en el uso de **Res**, el análisis de las incertidumbres contenidas en la matriz de correlación completa (**R**) no existe hasta ahora. Nosotros empleamos varias realizaciones para estimar las incertidumbres de los resultados de FWI. Nuestro enfoque lleva a construir la matriz **R** completa, que es al final, la cantidad que encierra toda la información asociada a las incertidumbres. Nos enfocamos en las incertidumbres relacionadas con las variaciones en los modelos iniciales de FWI, y proponemos un método para estudiar la matriz **R** completa, denominado Mapa de Densidad de Correlación, **D**. Al utilizar el mapa **D**, encontramos que las zonas de más alta incertidumbre en los modelos invertidos están cerca de las fuentes sísmicas, de las interfaces y de las fronteras artificiales. Destacamos que **D** puede servir como un complemento para el estudio y la estimación de incertidumbres en FWI.

KEYWORDS / PALABRAS CLAVE

Full Waveform Inversion | Resolution | Correlation Matrix |
Inversión de Onda Completa | Resolución | Matriz de Correlación |

AFFILIATION

^aInstituto de Física, Facultad de Ciencias Exactas y Naturales, Universidad de Antioquia UdeA, Calle 70 No. 52-21, Medellín, Colombia

^bInstituto de Geociencias da Universidade Federal da Bahia, Rua Barão de Jeremoabo s/n, Ondina Salvador.

*e-mail: anyeresatehortua@gmail.com

1. INTRODUCTION

Full waveform inversion (FWI), has become a very popular tool for the inversion of parameters from seismic data given its ability to face non-linear ill-posed inverse problems, [1]. FWI is a process where the wave velocity is estimated through an iterative procedure consisting in the comparison of simulated (synthetic) and observed (real) seismic data. This method started in the early 80's, [2]; [3]; it has been used for velocity estimation in several applications in 2D and 3D seismic situations ([1], Brossier et al. [4], Brenders et al. [5], Vigh et al. [6]) and, despite its well-known requirements of large computational resources, it has been broadly used in Engineering, Vigh et al. [6] and for crustal scale geophysical studies, [7].

For most practical applications, FWI is a gradient-based optimization scheme used to find the velocity model that best approaches the minimum of a misfit function. For example, some implementations use a quasi-Newton method such as **L-BFGS** [8], [9], to compute the search direction by successive approximations of the Hessian matrix, while adjoint methods are used to compute the misfit function gradients, Brossier et al. [4], [10]. One of the most important issues associated with the use of FWI is the so-called cycle skipping. Cycle skipping, [11], Boonyasiriwat et al. [12], appears when the maximum time shift between synthetic and observed data is larger than half a period. These phase shifts may affect the search for the minimum of the misfit function, avoiding the convergence of the method. One way to minimize cycle skipping effects is through the use of multiscale approaches, Boonyasiriwat et al. [12].

Although it is frequently ignored, an important ingredient of FWI is the quantification of uncertainties, which has been traditionally studied through the resolution matrix (**Res**) [1],[7],[13],[14],[15],[16], Abreo et al. [17]. Such notion relies on a quadratic approximation of the misfit function, leading to interpret the Hessian matrix as the inverse of the posterior covariance. This aimed at making the resolution analysis a practical task. The main sources of uncertainty in the inversion process are: its ill-posedness nature, the election of the initial model, the election of windowing frequencies in the multiscale procedure, the approximations made during the modeling of the propagation of waves, and the approximations to estimate the gradient of the misfit function. As many of the aforementioned sources of uncertainty are somehow dependent on the implementation, in this paper we focused on the uncertainties related to variation in the starting models, by proposing a method to infer information from the posterior covariance matrix.

The use of the resolution matrix (**Res**) for the quantification of uncertainties in FWI, has not been studied in depth as compared with other topics, [7]. For instance, uncertainty quantification is an excellent complement in the interpretation of tomographic images. The difficulty to use an overarching method for the quantification of uncertainties, is directly related to the non-linear nature of FWI. The theoretical treatment of such quantification was fully developed by Tarantola's formalism; however, its realistic applications involve a large number of parameters, making such formalism non-viable

from the current practical stand point. One remarkable work has been presented by [7]. The authors show, using a gaussian approximation and manipulation over the Hessian, a method for quantitative resolution analysis in FWI, which presents substantial improvements in computational efficiency and is applicable to any misfit function. In such approximation, the Hessian matrix can be interpreted as the inverse of the posterior covariance matrix, Cov^{-1} . Such interpretation was suggested by [18] only for inverse problems close to be linear.

[7] defined the diagonal elements $H_{ii}(z,x)$, of the Hessian matrix as the local resolution of the model parameter m_i at the position (z,x) ; likewise, it was stated that the off-diagonal $H_{ij}(z,x)$, for $i \neq j$, "encapsulate" the spatial dependencies between m_i and m_j at different positions x_i and x_j . They argued: "Large off-diagonal elements imply that the simultaneous perturbation of different parameters or in different regions can compensate each other, leaving the misfit function nearly unchanged".

In this work we used several (and independent) realizations of FWI to estimate the uncertainties in the outcome. This approximation leads to build a full covariance matrix, that is, the quantity that includes all the information associated to process uncertainty. The covariance matrix analyzed herein was obtained from a set of computational experiments. We chose a **2D** representation of the subsurface, and used synthetic data in 100 realizations of the seismic inversion. For each realization, we changed the initial model and obtained a data set to analyze uncertainties. First, we performed a classical standard deviation map (z,x) as a proxy of the uncertainty. Then, we developed the Density of Correlation (Density of Covariance) concept to study the uncertainties. To lay the foundations of the method, we show the full development on an unreal data set as a first approach. We think that the initial implementation of our method must be carried out on a well-known synthetic set of data to thus assess its main features and benefits.

This paper is organized as follows: We start in section 2 by setting the notation and the specific FWI engine used for statistical experiments. In section 3, we describe the way chosen to prepare the starting models, and a general overview of the methodology used in statistical experiments. We calculated and discussed the usual quantities, as the mean values and the standard deviations, in section 3.2. In section 3.3, we developed the concepts of density of covariance map and density of correlation map. This method enables the obtaining of data from the covariance and the correlation matrix. Through these concepts, a part of the information contained in the big covariance matrix, NP^2 , can be visualized and analyzed by using matrices of the size of the velocity models, NP . The results of the application of such method to the data obtained in the statistical experiments are presented and analyzed in section 4. Finally, the conclusions are addressed in section 5.

2. THEORETICAL FRAMEWORK

FWI ENGINE USED IN STATISTICAL EXPERIMENTS

We used a 2D representation of the subsurface, which is described by nz points along the z axis, and by nx points along the x axis. The distances between points are denoted by Δz , along the z axis, and by Δx , along the x axis. Every velocity model in this work is understood as a matrix of size $NP = nz \times nx$. Each velocity element will be associated to the physical position $(z_k, x_l) = (k \Delta z, l \Delta x)$. From a computational perspective, the velocity model of the subsurface will be symbolized by a vector $\mathbf{M} = (c_1, \dots, c_{NP})$, where each value c_i will be named as pixel. Each pixel of the vector \mathbf{M} will be equal to a value of the velocity field, in an ordered way such that $(k, l) \rightarrow c_{k+nz \cdot l}$, where the pair of indexes (k, l) will be understood as the position, in the computational mesh, of the pixel number $k + nz \cdot l$. A number ns of sound sources, with coordinates $(z_{si}, x_{si}) \forall_{i=1, \dots, ns}$, which generate the propagating waves are arranged. In all of our experiments, all sources are placed at the same depth $z_{si} \forall_{i=1, \dots, ns}$. The sources are separated by a distance ds , and arranged along the x axis. Together with the sources, a number nr of receivers, separated a fixed distance dr between them, are placed along the x axis at coordinates $(z_{ri}, x_{ri}) \forall_{i=1, \dots, nr}$. The observed data will be denoted by \mathbf{d}_o .

The pressure field is symbolized with $p(z, x, t)$. We used a Ricker's source function, $g(t) = \delta(z - z_s) \delta(x - x_s)$, defined by $g(t) = (1 - 2\pi^2 f_d^2 t^2 / \omega^2) e^{-\pi^2 f_d^2 t^2}$, with a dominant frequency $f_d = 15\text{Hz}$ for all the cases studied in this paper. All the experiments were done by using a numeric solution to the acoustic wave equation.

With such solution we propagate the pressure field in order to get the synthetic data \mathbf{d}_s . FWI makes a comparison between observed and synthetic data by iteratively minimizing an error function, denoted by E , estimated with a l_2 -norm. To ease the convergence of the method, a multi-scale approach has been employed.

The acoustic wave equation was solved by using the rapid expansion method (REM), [19], the pressure field is set at $t = 0$, for every point (z, x) , as $p = 0$ and $\partial_t p = 0$. The gradients $\nabla E(\mathbf{M})$ were calculated by using the Adjoint State Method described in [20]. In order to do the modeling of propagation of energy inside the finite $nz \times nx$ spatial domain, it is necessary to build artificial boundaries to simulate an infinite domain, and to avoid undesirable nonphysical reflections. To do this, we used Absorbing (Artificial) Boundary conditions.

The error function is evaluated for each iteration, as such evaluation is aimed at obtaining a good descent direction and making sure that the minimization procedure has been reached. We used the first Wolfe's condition, which is widely used with such procedure, [19], [21].

$$E(\mathbf{M}_{k+1}) \leq E(\mathbf{M}_k + \alpha_1 \alpha_k \nabla E(\mathbf{M}_k)^T \mathbf{h}_k), \quad (1)$$

where we used $\alpha_1 = 10^{-3}$ and $\alpha_0 = 1.0$. α_k is the step length that can be computed by a line-search algorithm [21]. \mathbf{h}_k is a search direction, usually determined by gradient methods, to find it we used **L-BFGS**. The minimization of the error function $E(\mathbf{M})$ around the neighborhood of the initial model \mathbf{M}_0 , is usually obtained through a Taylor's expansion of $E(\mathbf{M})$. By equating the derivative, respect \mathbf{M} , of such expansion to zero one gets the step descent [11].

$$\mathbf{M}_{k+1} = \mathbf{M}_k - H_k^{-1} \nabla E_k = \mathbf{M}_{k+1} = \mathbf{M}_k + \alpha_k \mathbf{h}_k \quad (2)$$

where H_k^{-1} is an approximation to the inverse of the Hessian matrix, in the k -th step of the inversion, evaluated in \mathbf{M}_0 . The exact Hessian matrix, is usually neglected due to its large size and high computational cost [22].

3. EXPERIMENTAL DEVELOPMENT

METHODOLOGY FOR THE SETUP OF INITIAL MODELS AND FOR THE EXPERIMENTS

We will use as exact data sets: The DiffraCTOR and the Marmousi velocity models, and these will be denoted as \mathbf{M}_{real} as shown in Figure 1. The term "real data" refers to exact data known in advance.

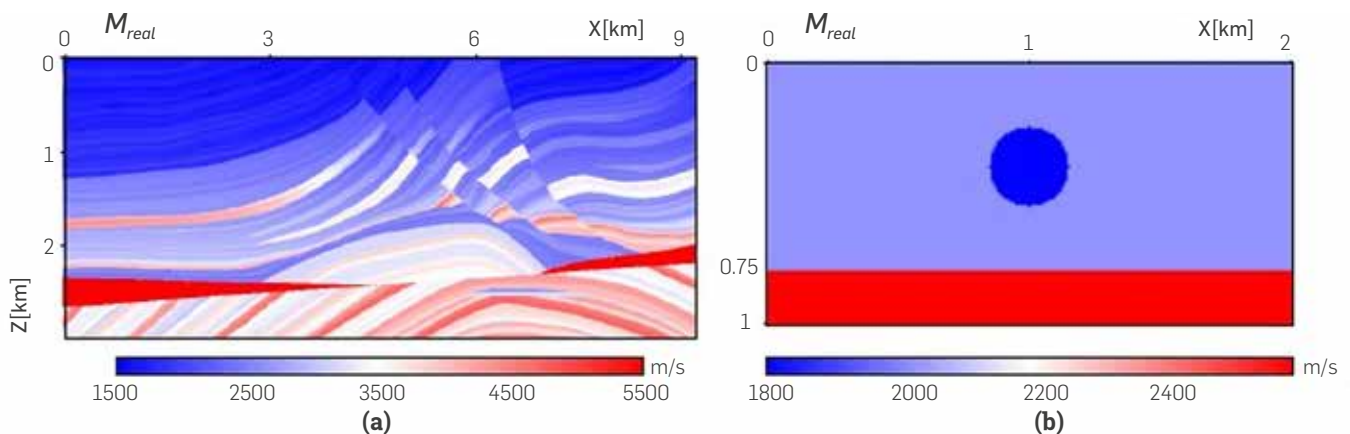


Figure 1. (a) Exact data set of Marmousi model. (b) Exact data set of the DiffraCTOR model.

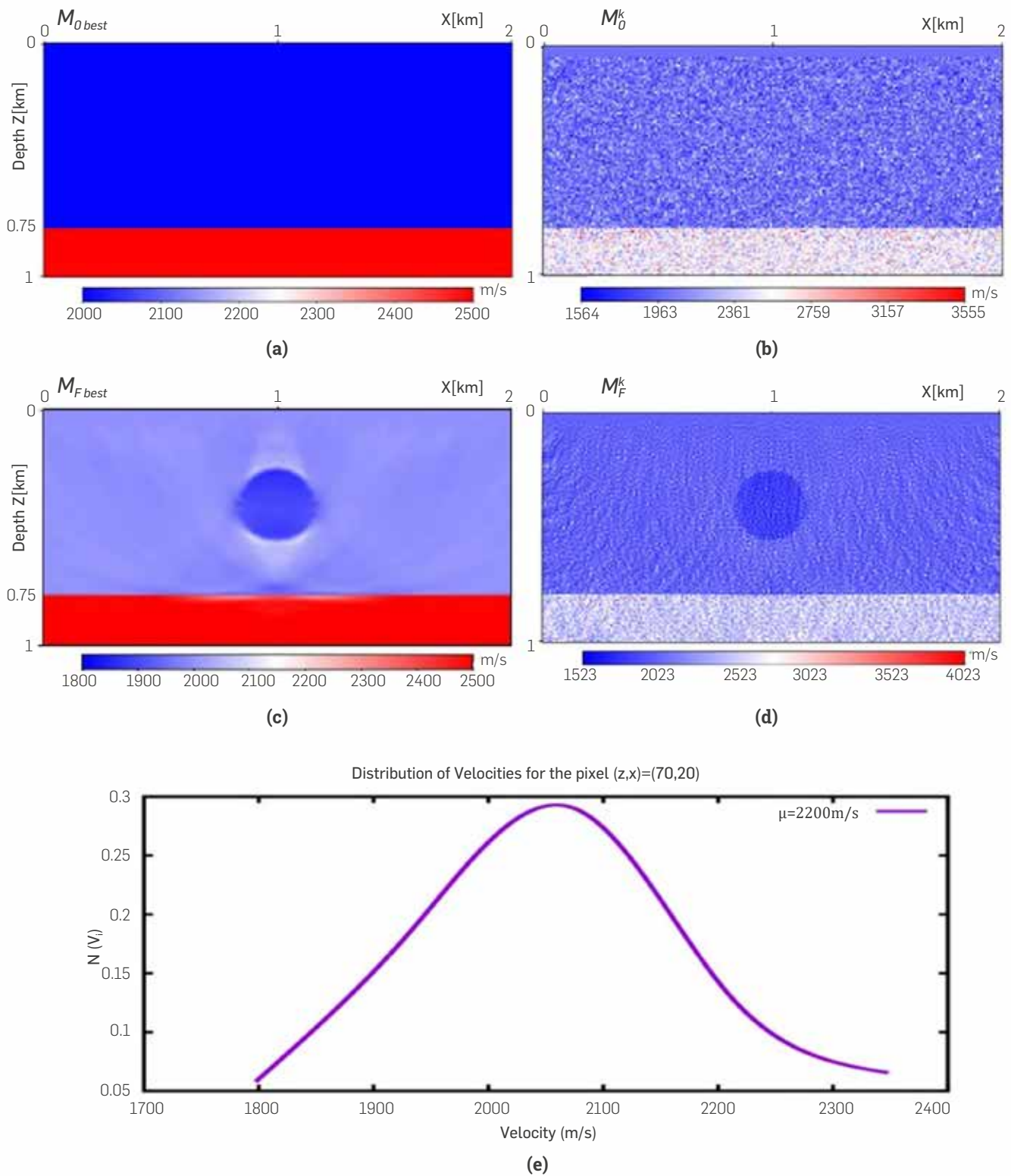


Figure 2. (a) The fiducial initial model, $M_{0_{best}}$ and its fiducial inverted model, $M_{F_{best}}$ in (c). A perturbed initial model, for $k=56$, M_0^k , and its FWI, M_F^k , are displayed in (b) and (d), respectively. (e) It shows (quasi-normal) the distribution of velocities of the initial models cube for the pixel (70,20).

Several initial models can be used as a starting point in FWI. This is supposing that fr ed from a smooth of the M_{real} of Figure 1a. Figure 3a contains letters A,B,C,D and E, pointing out several zones with relevant data from M_{real} , which helps the convergence of the FWI. This fiducial initial model will be the initial model to obtain the best outcome from the FWI process.

Now, let $\{M_0^k\}_{k=1}^{nm}$ be the collection of the nm possible starting models for the F W I. The i th pixel of the k th model, M_0^k , will be labeled by $c_{0,i}^k$. If the information from the geophysical methods is consistent and coherent with the existing geological data, the nm aforementioned initial models may be similar but not identical. This similarity, considering that the non-linearity involved in FWI usually requires a good starting model, allows to argue, as one of our working hypothesis, that for a given fiducial starting model $M_{0_{best}}$, the rest of possible initial models $\{M_0^k\}_{k=1}^{nm}$, for a "successful FWI", may lie "close" to $M_{0_{best}}$.

An initial model M_0^k ($M_0^k \neq M_{0_{best}}$) will be considered "close" to the $M_{0_{best}}$ if for i th pixel $c_{0,i}^k \in M_{0_{best}}$, the fractional difference with its corresponding i th pixel $c_{0,i}^{best} \in M_{0_{best}}$ is smaller than or equal to a predefined tolerance $perc$, namely:

$$\frac{|c_{0,i}^{best} - c_{0,i}^k|}{c_{0,i}^{best}} \leq perc, \forall i \in 1, \dots, NP \wedge \forall k \in 1, \dots, nm.$$

Thus, the $perc$ value, allows for a discrepancy limit between the values of the pixels in $M_{0_{best}}$ and any other possible initial model. Once a $M_{0_{best}}$ has been chosen, the remaining $nm-1$ initial models were built as random perturbations of the fiducial initial model. Each pixel $c_{0,i}^k$ of an initial model M_0^k was randomly generated as

$$c_{0,i}^k = c_{0,i}^{best} \pm Rand(0, perc * c_{0,i}^{best}), \forall i \in 1, \dots, NP \wedge \forall k \in 1, \dots, nm.$$

Where $Rand(a,b)$ accounts for a random number in the $range(a,b)$. Despite $M_{0_{best}}$ being obtained directly from the M_{real} , by making a smoothing, every initial model of the set $\{M_0^k\}_{k=1}^{nm}$, is uncorrelated and in section 4.5, the computational proof of this crucial fact, is shown explicitly. Such lack of correlation allows us to guarantee that every starting model in the experiment is independent and, therefore, the results of this work are unbiased.

The value of each of the pixels $c_{0,i}^k$ are within the interval

$$(c_{0,i}^{best} - perc * c_{0,i}^{best}, c_{0,i}^{best} + perc * c_{0,i}^{best})$$

In the experiments presented herein, we fixed $perc = 14\%$. To reach this number, we started changing $perc$ with different values, from 1% to 20% ; and $perc=14\%$ was the highest value for which FWI produced "successful" inversions. The highest values of $perc$ lead to dominant cycle skipping effects that affected, and in some cases avoided, the convergence of the inversion. We will refer to the

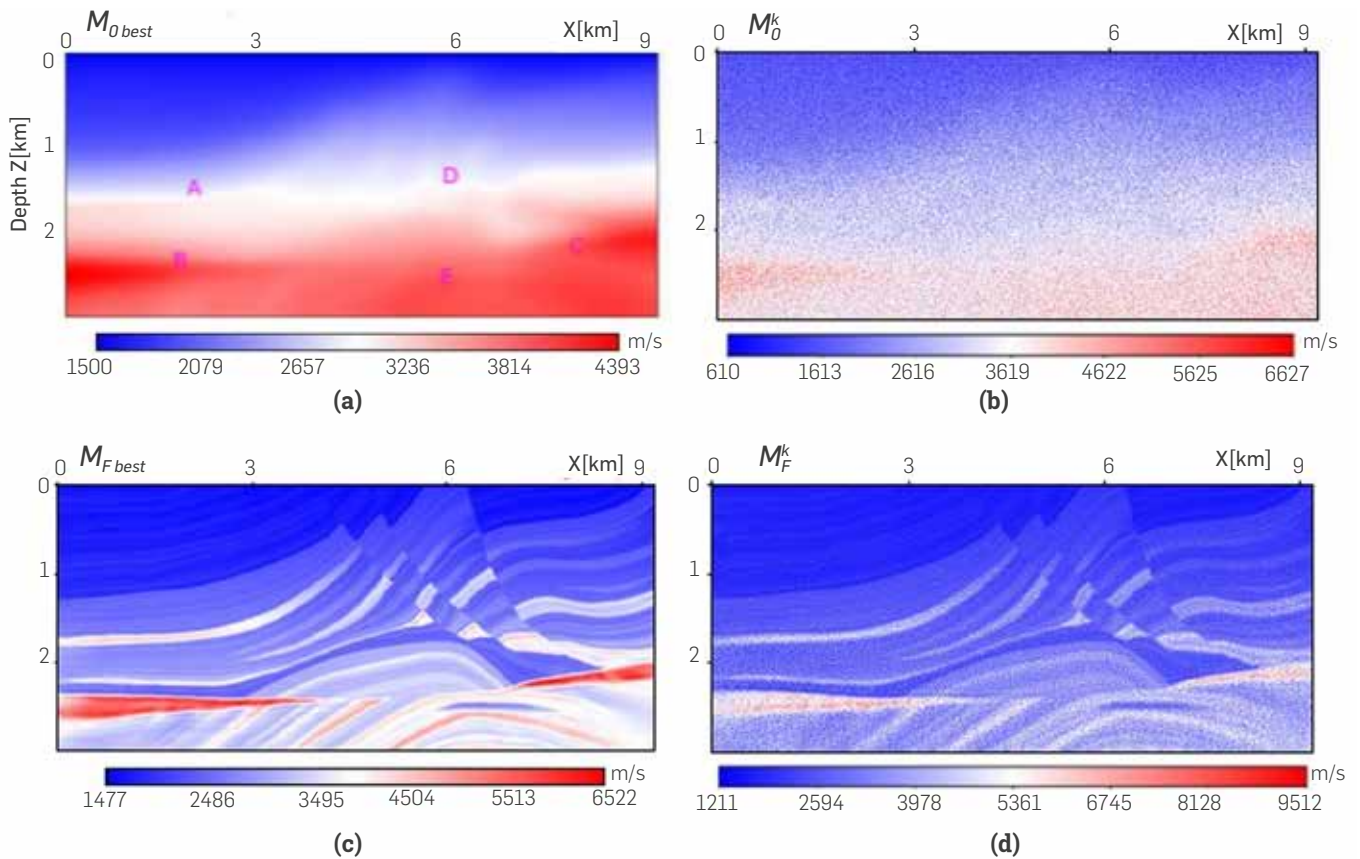


Figure 3. (a) The fiducial initial model, $M_{0_{best}}$, and its fiducial inverted model, $M_{F_{best}}$, in (c). A perturbed initial model, M_0^k , for $k=56$, and its FWI, M_F^k , are displayed in (b) and (d), respectively.

nm initial models built by using this procedure as “the perturbed models”. A perturbed model, with $k=56$, for Diffactor, is shown in **Figure 2b**, and for Marmousi in **Figure 3b**.

The fiducial inverted model $\mathbf{M}_{F\ best}$ with pixels $\bar{\mu}_i$, accomplished by applying FWI to $\mathbf{M}_{0\ best}$ is shown in **Figure 2c**, for the Diffactor model, and in **Figure 3c**, for Marmousi. The symbol \mathbf{M}_F^k is used for the k th model of the cube, that contains nm inverted models obtained by applying FWI to the k th perturbed model in \mathbf{M}_0^k , as shown in **Figures 2d** and **3d**, for Diffactor and Marmousi models, respectively. The set of final outputs, $\{\mathbf{M}_0^k\}_{k=1}^{nm}$ is used for quantifying the uncertainty of the velocity profiles.

The statistical experiment was carried out in the same way for the two models: Diffactor and Marmousi. The cube of nm initial models $\{\mathbf{M}_0^k\}_{k=1}^{nm}$, was inverted through FWI, by using synthetic data obtained from propagations in the \mathbf{M}_{req} and by using the frequencies, $(\omega_1, \omega_2, \omega_3, \omega_4)$, in the multiscale procedure for all models.

Figure 2e shows the distribution of velocities of the initial model cube for the pixel (70,20). It was confirmed that the distribution of every pixel, for both models, satisfied a quasi-normal distribution. Based on the quasi-normal distribution of the velocities and, based on the central limit theorem (which requires $nm \sim 30$), we are confident that $nm=100$ starting models represents a great sample for our experiment.

USUAL ANALYSIS OF THE UNCERTAINTY

The uncertainties of the FWI were analyzed using the nm final inverted models, taking the j th multivariate random variable as the vector $\mathbf{m}_j = (c_j^1, \dots, c_j^{nm})$. Thus, the final cube, \mathbf{M}_F , of inverted models can be considered a tensor $\mathbf{M}_F = (m_{j_1}, \dots, m_{j_{NP}})$.

$$\langle \mathbf{m}_j \rangle = \frac{1}{nm} \sum_{k=1}^{nm} c_i^k, \forall i = 1, \dots, NP. \quad (4)$$

The traditional quantification of uncertainties is made through the estimation of a map, $\sigma(z, x)$, of the standard deviations with a priori mean for each pixel $\bar{\mu}_i(z_i, x_i)$ as the square root of the variance

$$\sigma_{\bar{\mu}_i}^2(z_i, x_i) = \frac{1}{mn} \sum_{k=1}^{mn+1} (c_i^k - \bar{\mu}_i(z_i, x_i))^2. \quad (5)$$

DENSITY OF CORRELATION MAPS

The $\sigma(z, x)$ map is a method used to quantify uncertainties. However, it uses data only from the diagonal elements of the covariance matrix. Off diagonal terms of the covariance matrix may differ from zero, and if that is the case, important information can be extracted on the correlation induced between different elements of the velocity model. In this work, we estimated the covariance matrix as

$$\mathbf{cov}[c_i, c_j] = \frac{1}{nm-1} \sum_{k=1}^{nm} (c_i^k - \langle c_i \rangle)(c_j^k - \langle c_j \rangle), \quad (6)$$

Where each entry is an estimate of the relation of the velocity values of the two pixels c_i and c_j . It should be noted that this is a general estimation. No assumption about the nature of the underlying distribution of the uncertainty is made, and it is not a diagonal matrix. Indeed, it is possible that, without focusing on possible pathological

cases, if an entry $\mathbf{cov}[c_i, c_j]$ has a large absolute value, then the uncertainty is increased, as the distances $(c_i^k - \langle c_i \rangle)$ and $(c_j^k - \langle c_j \rangle)$ are large. Similarly, if it has a small absolute value, the uncertainty is expected to decrease.

Thus, the $\mathbf{cov}[c_i, c_j]$ matrix contains relevant information about the uncertainties that is not included in the analysis of the standard deviation map that only takes into account the self-correlation. To simplify the analysis, we will work with the correlation matrix \mathbf{R} , which we estimate as

$$R_{c_i, c_j} = \frac{\sum_{k=1}^{nm} (c_i^k - \langle c_i \rangle)(c_j^k - \langle c_j \rangle)}{\sqrt{\sum_{k=1}^{nm} (c_i^k - \langle c_i \rangle)^2} \sqrt{\sum_{k=1}^{nm} (c_j^k - \langle c_j \rangle)^2}}, \quad (7)$$

\mathbf{R} matrix carries the same information as covariance matrix, but this normalized form helps to understand, among other aspects: (a) How the wave velocities are correlated within a model. (b) The meaning of the correlation between velocities. (c) The relationships that exist between the correlation of the pixels and the uncertainties of the velocities associated with those pixels. The \mathbf{R} and covariance matrix contains data that is not usually analyzed in the description of the uncertainties in FWI. Maybe, a reason to keep it out of the discussion is related to its size. Since for a set of \mathbf{NP} random variables, \mathbf{R} is a \mathbf{NP}^2 sized matrix, the size of such data set becomes a challenge. For example, for the simple Marmousi model used in this work implies the requirement of 153Gb of memory in double precision, which is quite large for such a small model. Hence, a reliable estimate of uncertainties analysis for FWI turns to be expensive. In comparison, the methods that use the resolution matrix, opt for the Hessian, which dimension is \mathbf{NP} , and it requires less computational resources, although it contains less information. If we want to know more about the uncertainties in FWI, we must necessarily use more computational resources and all the information contained in \mathbf{R} .

We compute the \mathbf{R} matrix for both, the Diffactor and the Marmousi models. We visualize \mathbf{R} as a collection of NP sub-matrices, each one of size \mathbf{NP} . For example, the correlation matrix $\mathbf{R}_{c_{7580j}^i}, \forall j = 1, \dots, \mathbf{NP}$, will symbolize the sub-matrix of correlation of the pixel c_{7580}^i with the rest \mathbf{NP} pixels in the model. **Figure 4a** shows the matrix $\mathbf{R}_{c_{7580}^i}$.

The m th sub-matrix, \mathbf{R}_{c_i} , is a map with ordered elements $(\mathbf{R}_{c_i^1, c_i^1}, \dots, \mathbf{R}_{c_i^1, c_i^{NP}})$. The element $\mathbf{R}_{c_i^1, c_i^{k+nm \cdot j}}$ symbolizes the correlation of the pixel c_i^1 with the pixel $c_{k+nm \cdot j}^i$, where every value was computed using equation (7). Using this nomenclature, the kl -th element of the matrix \mathbf{R}_{c_i} , will be given by $\mathbf{R}_{c_i^1, c_i^{k+nm \cdot j}}$. **Figure 4a** shows the correlation map of submatrix $\mathbf{R}_{c_{7580}^i}$. The continuous blue band at the top of the map corresponds to the first 40m that were not inverted. The red point inside the circles shows that the pixel is completely self-correlated. In general, visualizing and extracting information from matrix \mathbf{R} is not trivial because of its large size. On the other hand, one might be interested in to see how strong is the correlation between a pixel and its close neighborhood. It is not actually expected to see any correlation between pixels that are too far away from each other. Therefore, to look for correlations between pixels, and in order to simplify the analysis of the information in the full matrix \mathbf{R} , we are proposing a method intended to accomplish these goals.

We propose to associate only one real number D_{c_i} , to each \mathbf{R}_{c_i} matrix. D_{c_i} will be named “The Density of Correlation” of the pixel c_i . Let $(p \Delta z, q \Delta x)$ be the physical position of the pixel c_i , see **Figure 4a**.

D_i is computed by averaging all values of the correlation inside a ring of width $\Delta=r_{n+1}-r_n$, for $n=0,1,\dots$; and center at $(p\Delta z, q\Delta x)$. Such an average is divided by the area of the ring. In this manner, each ring is labeled through an integer n : $n=0$ accounts for a circle containing the first neighbors only, $n=1$ label the first ring, and so on.

For example, the density of correlation of each pixel with its first neighbors, where the ring becomes a simple circle with $r_0=0$ and $r_1=\min(\Delta z, \Delta x)$, is estimated without including the self-correlation value, as

$$D_i = \frac{1}{N\pi r_1^2} \sum_{(k,l)}^N R_{c_i, c_{k+nz * l'}} \quad (8)$$

such that $|(p\Delta z, q\Delta x) - (k\Delta z, l\Delta x)| \leq r_1$, where N is the total number of correlation values inside the circle of radius r_1 .

It is expected, from the physical point of view, that the largest correlation of the pixel c_i , will be associated to its first neighbors, as the arriving wave to the pixel comes directly from such first neighbors. This physical fact was computationally explored, by analyzing the behavior of D_i as a function of n , which is shown

in Figure 4b. Let $A_n = \pi (r_n^2 - r_{n-1}^2)$ be the area of the n -th ring, then the quantity $|A_n D_i(n)|$ accounts for the absolute value of the average of the correlation values in the n -th ring. Figure 4b presents $|A_n D_i(n)|$ for the first 20 radial bins for $c_i = c_{37525}$ in the Marmousi model. It should be noted that the intensity of the correlation averaged for each ring decreases rapidly for the first 5 rings, regardless on the normalization effect of by the geometric factor A_n in equation (8). The same behavior was evidenced by all pixels in both velocity profiles. Thus, we confirmed that correlation is a local effect and the density of correlation D_i can be calculated for the first neighbors without compromising much data. Thus, by using D_i we have reduced the data of sub-matrix R_i into a number D_i representing the density of correlation of pixel c_i with its neighbors. Thus, the full data of the R matrix is reduced from a matrix of size NP^2 to a single matrix of size NP . The association of a number D_i with each R_i matrix, results in the concept of Density of Correlations Map $D_n(z, x)$, for a ring with a maximum radius r_n , defined by the collection $D_n(z, x) = \{D_1, \dots, D_{NP}\}$, and with units m^{-2} . Similarly, by using an identical analysis, we can define the Density of Covariance Maps $Cov_n(z, x)$, for which the equation (6) is used. The analysis presented in this work were built for the first neighbors, $n=0$, and then we will simplify the notation as $D_0(z, x) = D(z, x)$ and $Cov_0(z, x) = Cov(z, x)$.

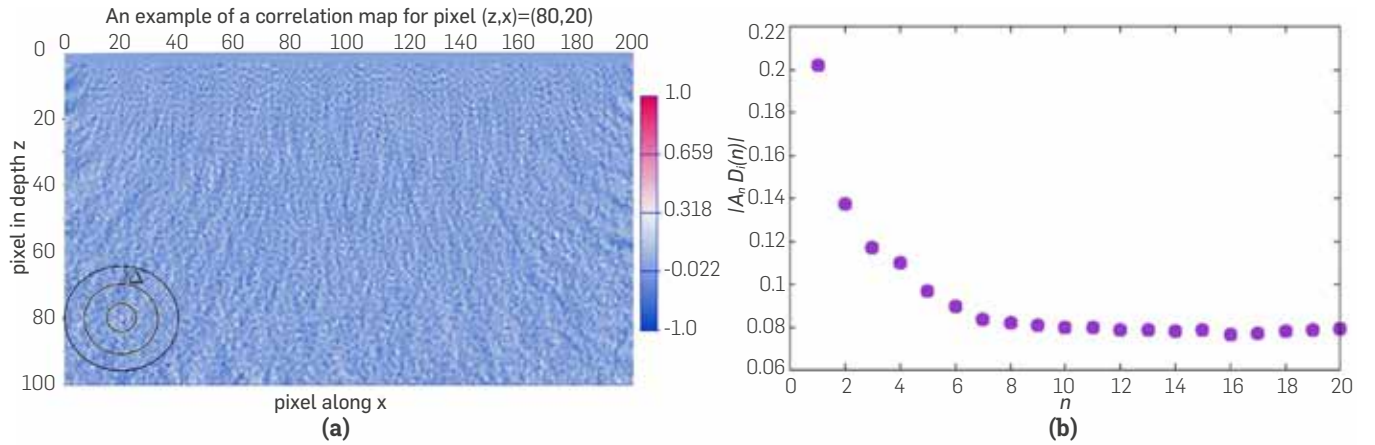


Figure 4. (a) Rings used to compute D_i , by averaging all values of the correlation inside a ring of width Δ , with center in the physical position of the pixel c_i , such average divided by the area of the ring. (b) $|A_n D_i(n)|$ as a function of distance, for the first 20 rings. The intensity of $|A_n D_i(n)|$ decreases rapidly. The same behavior was verified for all pixels in both velocity profiles.

4. RESULTS AND ANALYSIS

MEAN VALUES MAP $\langle M_F(z, x) \rangle$: DIFFRACTOR MODEL

The Diffactor model has the parameters $nz = 101$, $nx = 201$, $\Delta z = \Delta x = 10m$, and $NP = 20301$. The dimensions are $1km$ in depth, and $2km$ in x . In order to do every FWI, $ns = 11$ sources were disposed at $z_s = 40m$, and $x_{st} = (1000 \pm i * 200)m$, where $i=0,1,2,\dots,5$. A receiver is located at each grid point along the x axis, then $nr = 200$; and $z_r = 0m$. The frequencies $(\omega_1, \omega_2, \omega_3, \omega_4) = (10, 20, 30, 50)Hz$ were used in the multiscale, with 5 iterations for each frequency. This model consists on a first layer, $z \in [0, 750]m$, with a wave velocity of $2000m/s$ and a second layer, $z \in (750, 1000]m$, with a velocity of $2500m/s$. The first layer contains a circular object,

labeled as Diffactor, with a radius of $150m$, and centered at $(z_c, x_c) = (400, 1000)m$. The mean values map $\langle M_F(z, x) \rangle$, which was built using equation (4), is shown in Figure 5a. Figure 5b shows several vertical cuts at $x = 1000m$, a cut for $\langle M_F(z, x) \rangle$, a cut for the initial profile $M_{0_{best}}$, a cut for the real profile M_{real} and a cut for the fiducial inverted profile $M_{F_{best}}$. Although this figure is presented only for $x=1000m$, the features discussed hold for every x , as we verified cuts for $x=10m, 20m, \dots, 1990m$.

Note that the mean velocity (violet line) is closer to the real (blue line) than the inverted fiducial model (black line). Just inside the circular object and its surroundings, the difference between $M_{F_{best}}$ and M_{real} has the highest value. As a general observation, such

difference increases in the neighborhood of each interface, i.e., the interfaces are sources of uncertainty.

When the waves reach the zone $z > 750m$, they have crossed three boundaries: $z = 250m$, $z \sim 550m$, and $z \sim 750m$; and we note that the discrepancy between the different FWI shown in Figure 5b does not grow uniformly while depth increases. Thus, such discrepancy is low for $0m < z < 250m$, later the discrepancy increases inside the circular diffractor, and in the subsequent meters $250m < z < 750m$; and for $z > 750m$, the discrepancy decreases. However, such decrease does not mean a decrease of the uncertainty with depth, as Figure 5b does not show a standard deviation map. Figure 5b is merely a comparison of a FWI cut. In deeper positions, there is less illumination, and the physical consequences are shown as an increase of the uncertainty, see Figure 6b.

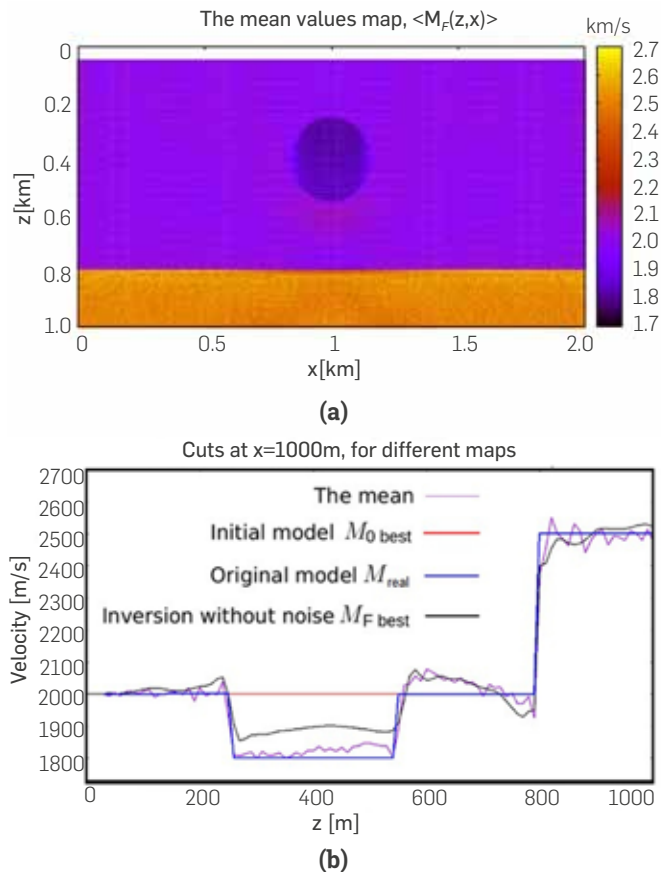


Figure 5. (a) The mean values map. (b) Comparison between the mean values map $\langle M_F(z,x) \rangle$, the initial profile M_{0_best} , the exact profile M_{real} and the best inverted profile M_{F_best} for $x=1000m$.

UNCERTAINTIES ON VELOCITIES: DIFFRACTOR MODEL

Figure 6a, measured in pixels, shows how the standard deviation increases with depth, having a jump just around $z \sim 0.75km \sim 80 pixels$. The zone $z \sim 0.75km$, $\sigma_{\mu}^-(z,x)$ shows the greatest contrast. This fact is a natural consequence of the little illumination reaching the bottom of the velocity profile. Just in the interface of the two layers, the uncertainty increases. This fact is in agreement with Figure 5b, where we argued that the discontinuities are a source of uncertainty.

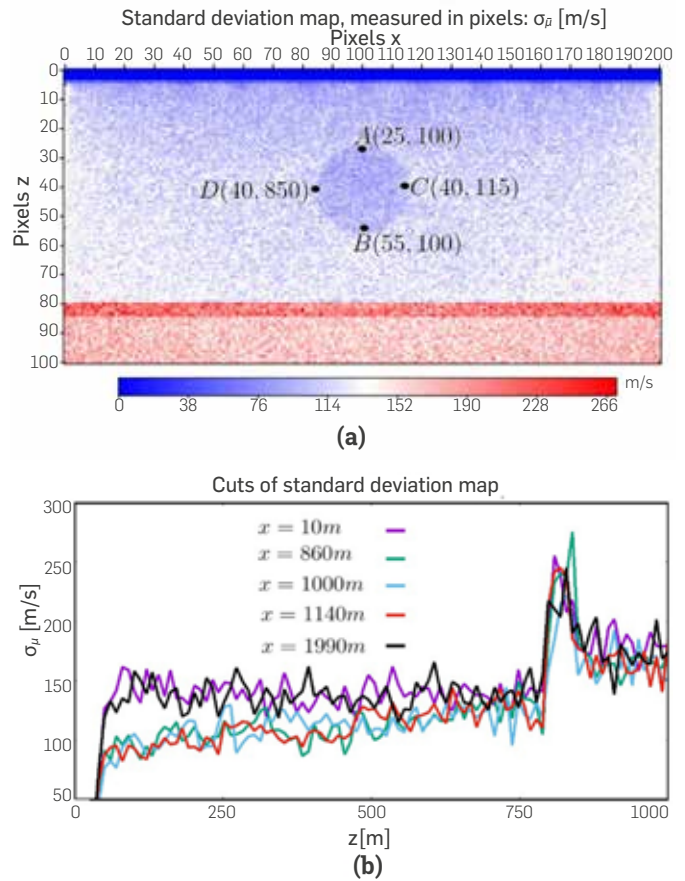


Figure 6. (a) The standard deviation map, with previous mean $\mu^-, \sigma_{\mu}(z,x)$ of inverted models $\{M_F\}$, resulting from FWI process. (b) Several cuts of the σ_{μ}^- , showing the increasing of the standard deviation with depth.

Figure 6b shows vertical cuts in the standard deviation map at different positions along the model. As it can be observed in the curves, there is a different behavior of the variation of uncertainty away from the circular diffractor than when it is close. Violet and black curves show that the standard deviations, $\sigma_{\mu}(z < 0.75km, x = 0.01km) \sim 150m/s$ $\sigma_{\mu}(z < 0.75km, x = 1.99km) \sim 150m/s$, close to the boundaries of the model, are larger than the standard deviations near the center, which are shown with blue, red and green curves. This fact is quite different inside the circular diffractor. Figure 6b clearly shows a global, systematic and almost linear increase of uncertainty with depth. An interesting fact related to FWI is that after a reflector (an interface), the variance decreases locally, i.e., the map $\sigma_{\mu}(z \sim 0.75km, x) \sim 250m/s$, and $\sigma_{\mu}(z > 0.75km, x) \sim 160m/s$; however $\sigma_{\mu}(z < 0.75km, x) \sim 120m/s$, i.e., such decreasing in merely local: $\sigma_{\mu}(z,x)$ always grows globally.

MEAN VALUES MAP $\langle M_F(z,x) \rangle$: MARMOUSI MODEL

All data about the Marmousi model used in this paper is available in the Madagascar repository [24]. This model lies under water approximately to 32m. It has 9.2km along x-axis, and 2.992km

along z -axis. It contains 158 horizontal layers and its extreme velocities are $c_{\min}=1500\text{m/s}$ and $c_{\max}=5500\text{m/s}$. The parameters used in this experiment were $nm = 100$, $nz = 375$, $nx = 369$, $\Delta x=0.025\text{km}$, $\Delta z=0.008\text{km}$. A receiver is located at each point along the x -axis, therefore, $n_r=369$; and $z_r=0\text{m}$. The number of sources is $n_s=62$, with $z_s=40\text{m}$, and $x_{s_i}=i*150\text{m}$, where $i = 0,1,2, \dots, 61$. The frequencies used in the multiscale were $(\omega_1, \omega_2, \omega_3, \omega_4) = (10, 20, 30)\text{Hz}$. In the inversion, 30 iterations per frequency were required, i.e., six times more than the number of iterations used for the Diffractor model. Thus, in order to reach $M_{F_{\text{best}}}$ the total time computation increases about 24 times as compared with the Diffractor model.

The mean values map $\langle M_F(z, x) \rangle$, for the Marmousi model is presented in Figure 7, as well as the lateral changes in velocity, belonging to $M_{F_{\text{best}}}$. Note that the complex zones, as those highlighted in white, circles and box, are recovered for the FWI.

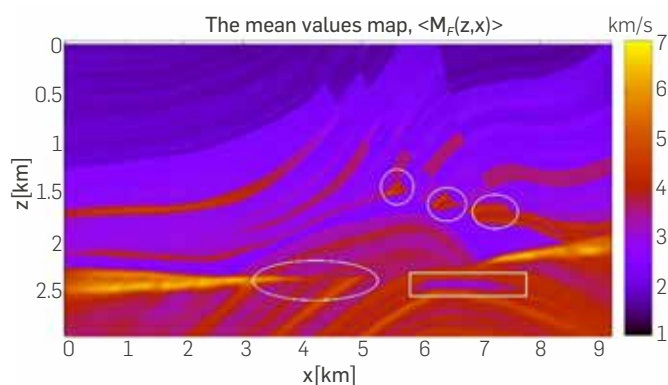


Figure 7. The mean values map, accomplished by doing FWI to the initial cube M_0 . Complex details of the model, as those highlighted in white, are present in both, $M_{0_{\text{best}}}$ and $\langle M_F(z, x) \rangle$.

Figures 8a and 8b show vertical cuts at $x=6.5\text{km}$ and horizontal cuts at $z=2\text{km}$, comparing the mean, the exact, the initial fiducial model, and the inverted fiducial model. In both figures the discrepancies between the results of the inversion are minor. Although the mean shows larger discrepancies as compared with the exact model than the $M_{F_{\text{best}}}$, a better quantification of such discrepancies may be revised in the standard deviation map, in order to check the places where the inversion introduces more uncertainty.

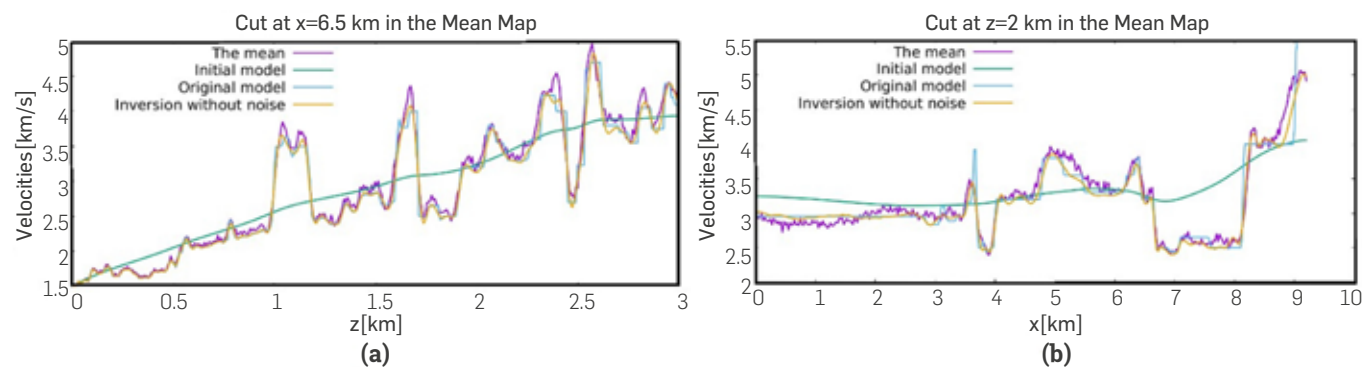


Figure 8. Comparison between the mean, the exact, the initial, and the inversion without noise, named $M_{F_{\text{best}}}$.

UNCERTAINTIES ON VELOCITIES: MARMOUSI MODEL

Figure 9a shows the standard deviation map. The zones with greater uncertainty are those with strong lateral variations in the velocity profile, for $2\text{km} < z < 2.5\text{km}$. Figure 9b shows the maximum uncertainty around 2.5km/s , for the cut $z=2.330\text{km}$. The exact velocity in this zone, with strong lateral changes, is 5.5km/s , and Figure 9c implies that the error for this zone is close to 45.45%, which is undesirable. However, only two zones show this behavior, and the rest of the map shows a standard deviation of $\sim 0.5\text{km/s}$, which is acceptable.

Figure 9c shows that the functional shape of $\sigma_{\mu}(z, x)$ has a global linear growth of uncertainty. The slope for the cuts is close to 2.34s^{-1} . Considering the detail of the fluctuations shown in Figure 9c, it is evident that the uncertainty has strong fluctuations in the region $2\text{km} < z < 2.5\text{km}$, where there are strong discontinuities in the profile as observed in Figure 9a.

Going back to the same behavior observed in the case of the Diffractor, we notice that when there are strong discontinuities in the medium, uncertainty grows locally in the region of the discontinuity. After seeing this effect on the artificial model of the Diffractor, and in this more realistic situation of Marmousi, we suggest that this increased uncertainty may be caused by the behavior of the modeling of waves in such discontinuities, where caustics of waves may appear due to the modeling of interfering waves in these regions. Note that once discontinuities are overcome, in region $z > 2.5\text{km}$, the standard deviation collapses, for all vertical cuts, to the same regular behavior.

ANALYSIS OF DENSITY OF CORRELATION FOR THE DIFFRACTOR MODEL

We now move to the Density of Correlation and Density of Covariance maps. To make sure that the experiment is unbiased, we show in Figures 10a and 10b the absolute value of the density of correlation $|D(z,x)|$ of the initial cubes M_0 , for the Diffractor and Marmousi models. From Figures 10a and 10(b), it can be observed that there is neither a preferred direction nor systematic fluctuations in the initial conditions map, which means that the random noise, introduced to each pixel in our experiment, leads to independent and uncorrelated initial models even when the $M_{0_{\text{best}}}$ comes from a smoothing of the M_{real} .

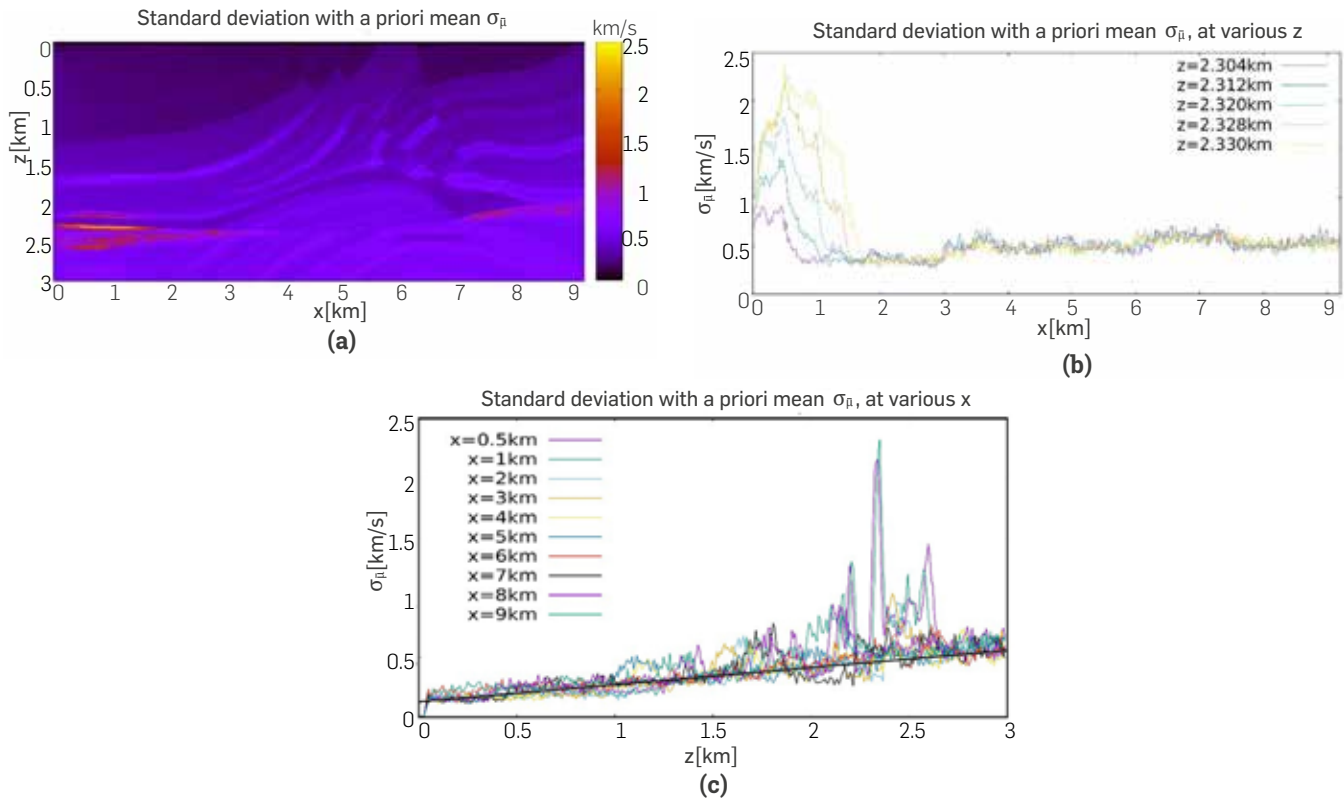


Figure 9. (a) The standard deviation $\sigma_{\pi}(z, x)$, of the inverted cube M_{π} , resulting from the FWI to the cube M_0 . (b) Several cuts for the zones with greater uncertainties, which is caused by the strong lateral gradients. Not considering the large peaks at $2\text{ km} < z < 2.5\text{ km}$, the functional shape $\sigma_{\pi}(z, x)$, is, on average, a line whose slope is around 2.34s^{-1} ; as is shown in (c).

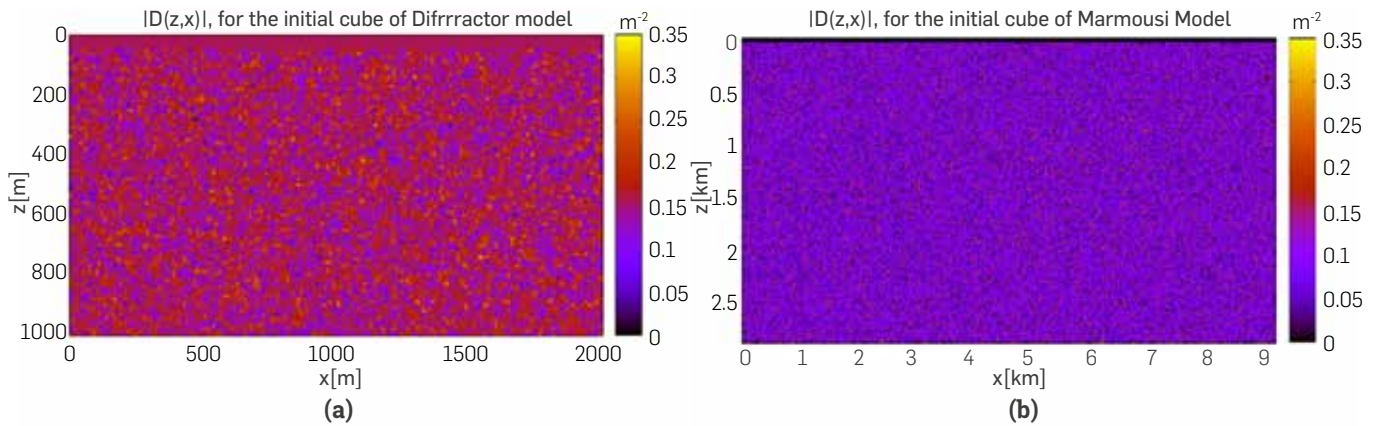


Figure 10. $D(x, z)$ for the initial models. (a) for the Diffractor, and (b) for the Marmousi. The maps show a uniform distribution of the Density of Correlation indicating non-biased initial data.

Figure 11a shows the absolute value of the Density of Correlation map, and Figure 11b shows the square root of the Density of Covariance map. It may be noticed that, although major structural features (as discontinuities) can be observed in both maps, the different normalization enhances diverse characteristics in each. For example, in the $\sqrt{\text{Cov}(z, x)}$ map, Figure 11b, the discontinuities of circular diffractor and the change of layer than in Figure 11a are clearer, whereas the white rectangle does not contain such change,

and the circular diffractor is diffuse. Comparing 11a and 11b, it can be observed that in the $|D(z, x)|$ map (see the green squares), it is easier to observe the artifacts (noise in the correlation) on the borders, due to the boundary conditions. Figure 12a shows vertical cuts at different positions at the borders and the center of the profile. Violet and green lines show, in agreement with what is seen in Figure 11a, that there is a low correlation between pixels at the border, $|D(z, x)|_{\text{max}} \sim 0.2\text{ m}^{-2}$. The correlation in this region, $x \sim 10\text{ m}$ or

$x \sim 1000m$, decreases as a function of distance from the surface falling down almost to zero at around $600m$. We suggest that the behavior of the correlation of pixels close to the borders may be related to the effect of boundary conditions, indicating that they behave partially as a reflector. In the region of the middle of the model (blue line) of Figure 12a, we can see that the density of the correlation is bigger, $|D(z,x)|_{max} \sim 0.5m^{-2}$, and it systematically decreases with z . This last behavior matches the findings of the analysis of standard deviation maps, where standard deviation increases smoothly with depth.

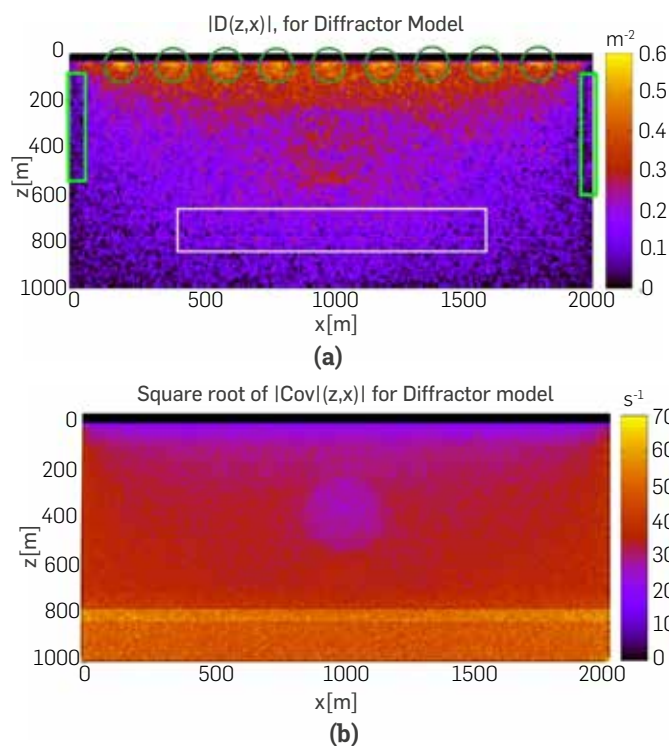


Figure 11. (a) $|D(x,z)|$ for Diffraction model. A decrease of uncertainty in well illuminated zones is evidenced through the increase of the values of Density of Correlation, which are near to the sources in the $D(x,z)$. The white rectangle highlights a limited definition of the interfaces, unlike to a better definition shown in (b), where $\sqrt{|Cov(x,z)|}$ is illustrated.

An important feature of the Density Correlation map, $|D(z,x)|$, is the possibility to observe the positions of the sources through the peaks of correlation, which are highlighted with green circles in Figure 11a. Thus, there are peaks in the correlation due to the presence of the sources. Remember that, for the Diffraction model, the 11 sources were disposed at $x_s = \{0, 200, 400, 600, 800, \dots, 1800, 2000\}m$. The effects of the boundaries mask the first and the last peak, corresponding with $x_s = 0m$ and $x_s = 2000m$. Thus, $D(z,x)$ shows that there is a strong correlation between the sources and its neighborhood. Assessing how this correlation affects the quality of the inversion is out of the scope of this work, but this diagnostic can be used to study the impact of the configuration of seismic sources on the final result of FWI. If we consider that large correlations are associated to small uncertainties (small cross-deviations from the mean value) it also implies that modeling the source is a key ingredient in FWI. The fact that the correlation can be other than zero in certain zones suggests the existence of physical data correlating the elastic properties of the pixels in the subsurface model. Such physical data comes from the seismic data, both \mathbf{d}_o and \mathbf{d}_c . These two data vectors contain relevant information on physical relations between different pairs of pixels inside the model and, therefore, $D(z,x)$ is large when there is a high correlation of those vectors. Obviously, close to the surface there is physical data available that correlates pixel values. For example, the correlation ϑ of the observed and modeled data has been described by [23] as:

$$\vartheta[\mathbf{d}_c, \mathbf{d}_o] \approx \int dt' \mathbf{d}_c(t + t') \mathbf{d}_o(t'). \quad (9)$$

The cuts shown in Figure 12b agree with equation (9), having peaks around the sources, where the observed and synthetic data share the greatest amount of available information. Thus, the procedure to analyze the correlation matrix through the Correlation Density maps reproduce natural facts as the correlation between synthetic and observed data. The $D(z,x)$ maps provide information on uncertainties around the sources that is not evident in the other two maps: The Standard Deviation $\sigma(z,x)$ or The Density of Covariance $Cov(z,x)$.

So far we have stated that the correlation between two different points suggests that their uncertainties are related, but such relation (the functional shape) is unknown and, therefore, an uncertainty analysis of the three maps, $\sigma(z,x)$, $Cov(z,x)$, and $D(z,x)$, may be used.

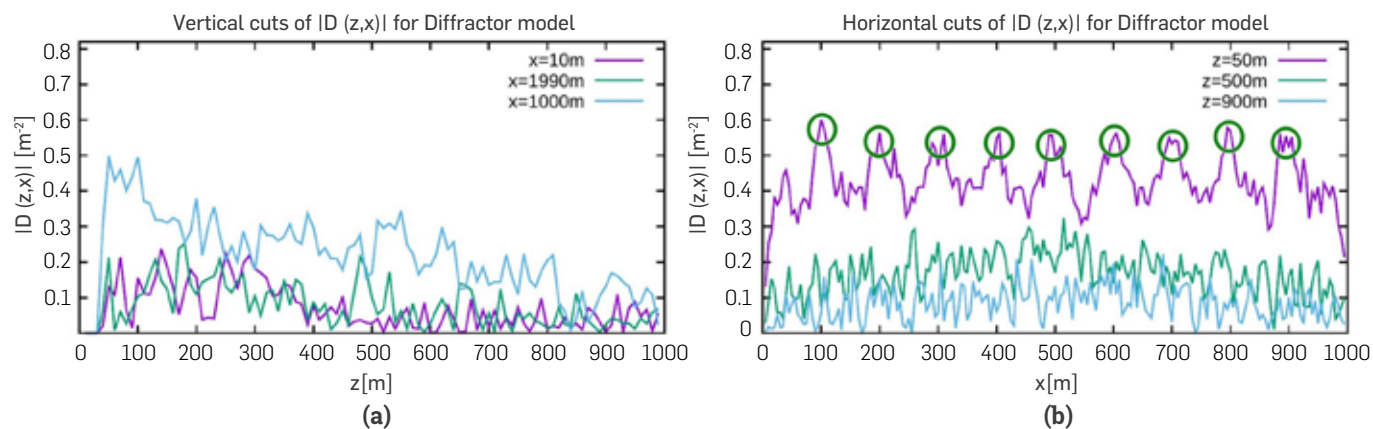


Figure 12. (a) Vertical cuts of $|D(x,z)|$ at different horizontal positions. (b) Horizontal cuts at different depths. The circles show the 9 peaks, corresponding to the sources, showing that the energy sources correlation with the pixels.

DENSITY CORRELATION ANALYSIS FOR THE MARMOUSI MODEL

The $Cov(z, x)$ and $D(z, x)$ maps were computed for the Marmousi model, which show similar results to those discussed for the Diffactor. In the $Cov(z, x)$, the decrease of uncertainties derived from the effects of boundaries was verified. However, due to the complexity of this model, the range of values of this map oscillates in the range $[0, 300^2] \text{ m}^2/\text{s}^2$; such an interval is very large and, therefore, the visualization of the information is somewhat unclear. To better visualize this map, we include its square root, $\sqrt{Cov(z, x)}$, in Figure 13a. Using this scaling, the contrasts are larger and it is possible to observe that, besides the boundaries, in the zones with high lateral gradients of velocity, the covariance (the uncertainties) increases. Figure 13a reveals that there are several physical or geometric features, other than illumination, which increase the uncertainties. Figure 13a shows zones enclosed in white squares and rectangles, and also zones pointed at with white arrows. The two smaller arrows point towards zones with $Cov(z, x) \sim 200 \text{ m/s}$, with depths $z \sim 1.5 \text{ km}$, while the smallest rectangle, with $Cov(z, x) < 100 \text{ m/s}$, is deeper $z \sim 1.9 \text{ km}$. The same phenomenon exists for the larger white arrow, which points to the highest wedge ($z \sim 2.5 \text{ km}$) associated to $\sqrt{Cov(z, x)} \sim 250 \text{ m/s}$, while the white squares point to zones ($z \sim 2.7 \text{ km}$) associated to $\sqrt{Cov(z, x)} \sim 130 \text{ m/s}$. Beyond the illumination, the physical (geometrical) properties of the model and the properties of the ingredients of the FWI engine produce quantifiable changes in the uncertainties. Such ingredients were described in section 2. The $\sqrt{Cov(z, x)}$ map and its properties are very similar to the mean value map $\langle M_r(z, x) \rangle$, see Figure 7. This fact comes from the contrast of velocity magnitudes, which are reflected in the $\sqrt{Cov(z, x)}$ map.

The mathematical standard deviation concept is close to that of the covariance map square root; therefore, the $\sqrt{Cov(z, x)}$ map is practically identical to the $\sigma_\mu(z, x)$ map, see Figure 9a. Such similarities enable relying on the algorithm and the method used to compute $Cov(z, x)$ and $D(z, x)$. An important fact to note, which is valid for all the cases studied herein, is that the Density of Covariance (coming from all elements of the matrix $\mathbf{cov}[c_i, c_j]$) differ from zero almost everywhere. This means that not all information of uncertainty in FWI is in the $\sigma_\mu(z, x)$ map (which comes from diagonal of $\mathbf{cov}[c_i, c_j]$), since σ_μ contains numerous values close to zero, see Figure 9a.

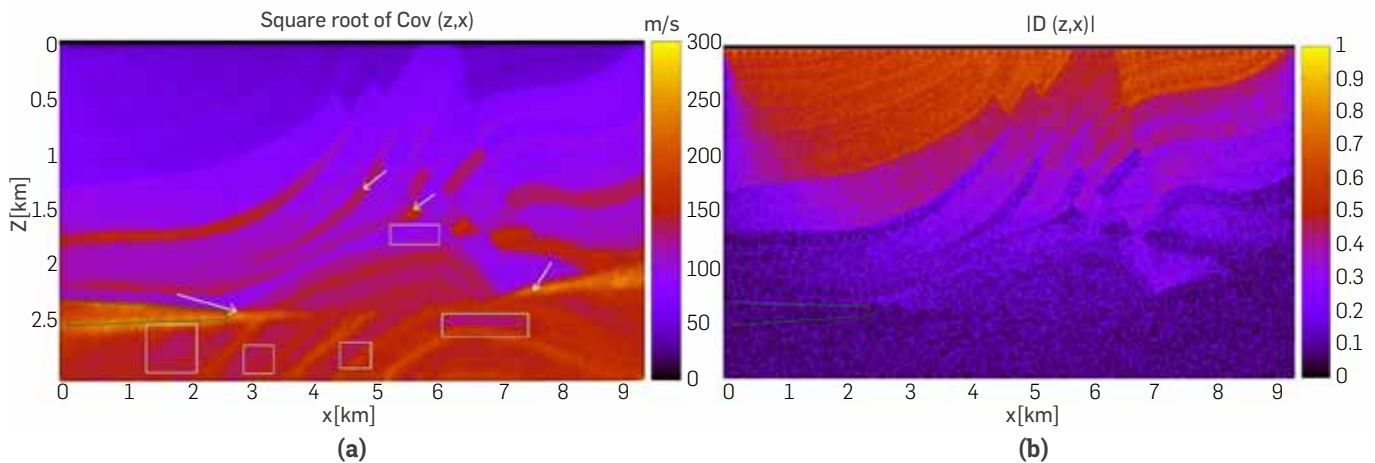


Figure 13. (a) $Cov(z, x)$ map of Marmousi model. There are several physical or geometric features, other than illumination, which increase uncertainties. (b) The $|D(z, x)|$ map containing 61 peaks, with correlation values close to 1, and corresponding with the positions of the sources.

Figure 13b shows the absolute value $|D(z, x)|$ map. Once again, it can be noted that for those zones with large uncertainties (large $Cov(z, x)$), the correlation density values are close to zero. The growth of the uncertainties coming from different causes with depth, is verified again. Zones such as those enclosed by green lines reinforce the interpretation of section 3.3: zones of $Cov(z, x)$, where the covariance increases entails zones of $D(z, x)$, where the uncertainties grow. From a general perspective, the $|D(z, x)|$ map reproduces the main features found for its analogous in the Diffactor. The uncertainties grow with depth and with proximity to the boundaries. Also, Figure 13b, contains 61 peaks with correlation values close to 1, and corresponding with the positions of the sources $(z_s, x_s) = (0.004, i * 0.15) \text{ km}$, with $i=0, 1, \dots, 61$. As it was already highlighted, the correlation density map can determine the correlation between the sources and the model.

CONCLUSIONS

Several realizations of FWI were used in this work to estimate the uncertainties in FWI, without having to rely on the classical quadratic approximation. We propose a new method to study the uncertainties in FWI through the estimation of the Density of Correlation/Covariance Map. To build the method, we propose measuring the density of the values of correlation/covariance, in the full \mathbf{R} matrix, relative to the first neighbors of each pixel.

The possibility to determine the Density of Correlation/Covariance only from the first neighbors enables calculation without major computational resources, inasmuch as the $D(x, z)$ map allows to reduce the correlation matrix of size NP^2 to one map of the size NP . From this map, we can obtain information on the correlation of a pixel of the medium with its first neighbors. A reduction of size in the matrices leads to the potential application of the analysis presented herein on real data. To lay the foundations of the method, we present all developments on unreal data set as a first approach. We consider that the initial implementation of our method must rely on a well-known synthetic set of data to evaluate its main features and benefits.

By using the $D(x, z)$ map, the $Cov(z, x)$, and the typical $\sigma_\mu(z, x)$ map, it is possible to propose a framework for the study and

estimation of uncertainties in FWI. Concerning uncertainties in the FWI, our analysis shows some interesting results:

- We found that $D(x,z)$ can be used to study the effect of implementation of boundary conditions. Since our procedure allows to recover the positions of the sources, it is worth studying the configuration of the sources.
- We have also found that velocity contrasts in the medium are some of the main sources of uncertainty. By using the concept of $D(x,z)$, the natural systematic increase of uncertainty with depth can be shown and quantified. Such quantification shows an almost linear increase of the uncertainty with depth and with the presence of the reflectors, especially with the lateral variations of the velocity profile.

■ We propose an uncertainty analysis that can be used, as a priori information, to impose limits to the parameter space in a seismic inversion procedure, as proposed by Tarantola. Apart from the natural applications that the density of correlation or covariance may have on the interpretation of FWI results, one can think on the implications of the estimation of the Density of Correlation or Covariance during the execution of the FWI. Computing these quantities on-the-fly during the execution of FWI may help to constrain the behaviour of the inversion using the estimated uncertainties as a proxy to explore the parameter space. This is an idea that is worth to be explored.

ACKNOWLEDGEMENTS

The authors acknowledge the financial support provided by the Colombian Oil Company ECOPETROL and COLCIENCIAS as part of research project grant No. 0266-2013. The authors are grateful to Reynam Pestana, from CPGG/UFBA, for their help with the Seismic data generation. Thanks to "Estrategia de Sostenibilidad, Universidad de Antioquia". Simulations were generated using the Madagascar package (<http://www.ahay.org>).

REFERENCES

- [1] Biswas R, Sen M (2017) 2d full-waveform inversion and uncertainty estimation using the reversible jump Hamiltonian Monte Carlo. SEG Technical Program Expanded Abstracts, DOI <https://doi.org/10.1190/segam2017-17680416.1>
- [2] Lailly P (1983) The seismic inverse problem as a sequence of before stack migrations. In: Bednar JB, Redner R, Robinson E, Weglein A (eds) Conference on inverse scattering: theory and application, SIAM, pp 206-220
- [3] Tarantola A (1984) Inversion of seismic reflection data in the acoustic approximation. Geophysics, 49(8):1259-1266
- [4] Brossier R, Operto S, Virieux J (2009) Seismic imaging of complex structures by 2d elastic frequency-domain full-waveform inversion. Geophysics, DOI <https://doi.org/10.1190/1.3215771>
- [5] Brenders A, Albertin U, Mika J (2012) Comparison of 3d time- and frequency-domain waveform inversion: Benefits and insights of a broadband, discrete-frequency strategy. SEG Technical Program Expanded Abstracts, DOI <https://doi.org/10.1190/segam2012-1299.1>
- [6] Vigh D, Starr B, Kapoor J, Li H (2010) 3d full waveform inversion on a gulf of Mexico waz data set. SEG Technical Program Expanded Abstracts, DOI <https://doi.org/10.1190/1.3513935>
- [7] Fitchner A, Trampert J (2011) Resolution analysis in full waveform inversion. Geophys J Int, DOI <https://doi.org/10.1111/j.1365-246X.2011.05218.x>
- [8] Nocedal J (1980) Updating quasi-Newton matrices with limited storage. Mathematics of Computation, 35(151):773-782
- [9] Liu D, Nocedal J (1989) On the limited memory BFGS method for large scale optimization: Mathematical Programming. Springer, DOI <https://doi.org/10.1007/BF01589116>
- [10] Brossier R, Operto S, Virieux J (2010) Which data residual norm for robust elastic frequency-domain full waveform inversion? Geophysics, DOI <https://doi.org/10.1190/1.3379323>
- [11] Virieux J, Operto S (2009) An overview of full-waveform inversion in exploration geophysics. Geophysics, DOI <https://doi.org/10.1190/1.3238367>
- [12] Boonyasriwat C, Valasek P, Routh P, Cao W, Schuster G, Macy B (2009) An efficient multiscale method for time-domain waveform tomography. Geophysics, DOI <https://doi.org/10.1190/1.3151869>
- [13] Kennett B, Nolet G (1978) Resolution analysis for discrete systems. Geophys J R astr Soc, 53:413-425
- [14] Williamson P (1991) A guide to the limits of resolution imposed by scattering in ray tomography. Geophysics, DOI <https://doi.org/10.1190/1.1443032>
- [15] Meles G, Greenhalgh S, Maurer H, Green A, van der Kruk J (2012) Gpr full-waveform sensitivity and resolution analysis using an ftdt adjoint method. IEEE Transactions on Geoscience and Remote Sensing, DOI 10.1109/IWAGPR.2011.5963863
- [16] Tao Y, Sen M (2013) Frequency-domain full wave inversion with scattering-integral approach and its sensitivity analysis. Journal of Geophysics and Engineering, DOI 10.1088/1742-2132/10/6/065008
- [17] Abreo, S. A., Ramírez- Silva, A. B., & Reyes- Torres, O. M. (2018). A GPU implementation of the second order adjoint state theory to quantify the uncertainty on FWI results. CT&F - Ciencia, Tecnología Y Futuro, 8(2). <https://doi.org/10.29047/01225383.86>
- [18] Tarantola A (2005) Inversion Problem Theory and methods for model parameter estimation. SIAM
- [19] dos Santos A, Pestana R (2015) Time-domain multiscale fullwaveform inversion using the rapid expansion method and efficient step-length estimation. Geophysics, DOI <https://doi.org/10.1190/geo2014-0338.1>
- [20] Plessix RE (2006) A review of the adjoint-state method for computing the gradient of a functional with geophysical applications. Geophysical Journal International, DOI <https://doi.org/10.1111/j.1365-246X.2006.02978.x>
- [21] Nocedal J, Wright SJ (2006) Numerical optimization, 2edn. Springer
- [22] Ma Y, Hale D (2012) Quasi-newton full-waveform inversion with a projected hessian matrix. Geophysics, DOI <https://doi.org/10.1190/geo2011-0519.1>
- [23] Leeuwen TV, Mulder WA (2010) A correlation-based misfit criterion for wave-equation traveltime tomography. Geophysical Journal International, DOI <https://doi.org/10.1111/j.1365-246X.2010.04681.x>
- [24] Madagascar Development Team (2012) Madagascar Software, Version-1.4. <http://www.ahay.org/>



Differentiating technologies **FOR MITIGATING** fuels' theft

Tecnologías diferenciadoras **PARA MITIGAR** el hurto de combustibles

- We have a suite of patented technologies in five countries that have contributed to losses due to **theft reduce by +95%.**
- We licensed the technology in Mexico.
- Distinctive capacity to negotiate with the operators.
- Theft associated losses worldwide exceed **USD\$100 trillion** per year (*).

* For losses and for investments in solutions to the problem.

- Contamos con una suite de tecnologías patentadas en cinco países que contribuyeron a reducir en **+95% las pérdidas por hurtos.**
- Licenciamos la tecnología a México.
- Capacidad diferenciadora para negociación con operadoras.
- Pérdidas por hurtos en el mundo superan los **USD\$100 billones** por año (*).

* Por pérdidas y por inversiones en soluciones al problema.